

*Accepted for publication by Publications of the Astronomical Society of the Pacific on 20/05/2008*

## **XPOL — the correlation polarimeter at the IRAM 30m telescope**

C. Thum, H. Wiesemeyer<sup>1</sup>

*Institut de Radio Astronomie Millimétrique, Domaine Universitaire de Grenoble, 300 Rue de la Piscine, 38406 St. Martin-d'Hères, France*

G. Paubert and S. Navarro

*Instituto de Radio Astronomía Milimétrica, Núcleo Central, Avd. Divina Pastora No. 7–9, 18000 Granada, Spain*

and

D. Morris

*Institut de Radio Astronomie Millimétrique, Domaine Universitaire de Grenoble, 300 Rue de la Piscine, 38406 St. Martin-d'Hères, France*

### **ABSTRACT**

XPOL, the first correlation polarimeter at a large millimeter telescope, uses a flexible digital correlator to measure all four Stokes parameters simultaneously, i.e. the total power  $I$ , the linear polarization components  $Q$  and  $U$ , and the circular polarization  $V$ . The versatility of the backend provides adequate bandwidth for efficient continuum observations as well as sufficient spectral resolution (40 kHz) for observations of narrow lines. We demonstrate that the polarimetry specific calibrations are handled with sufficient precision, in particular the relative phase between the Observatory's two orthogonally linearly polarized receivers.

The many facets of instrumental polarization are studied at 3mm wavelength in all Stokes parameters: on-axis with point sources and off-axis with beam maps. Stokes  $Q$  which is measured as the power difference between the receivers is affected by instrumental polarization at the 1.5% level. Stokes  $U$  and  $V$  which are measured as cross correlations are very little affected (maximum sidelobes 0.6%

---

<sup>1</sup>present address: Instituto de Radio Astronomía Milimétrica, Núcleo Central, Avd. Divina Pastora No. 7–9, 18000 Granada, Spain

( $U$ ) and 0.3% ( $V$ )). These levels critically depend on the precision of the receiver alignment. They reach these minimum levels set by small ellipticities of the feed horns when alignment is optimum ( $\lesssim 0.3''$ ). A second critical prerequisite for low polarization sidelobes turned out to be the correct orientation of the polarization splitter grid. Its cross polarization properties are modeled in detail.

XPOL observations are therefore limited only by receiver noise in Stokes  $U$  and  $V$  even for extended sources. Systematic effects set in at the 1.5% level in observations of Stokes  $Q$ . With proper precautions, this limitation can be overcome for point sources. Stokes  $Q$  observations of extended sources are the most difficult with XPOL.

*Subject headings:* Astronomical Instrumentation — Quasars and Active Galactic Nuclei

## 1. Introduction

Spectropolarimetric observations at millimeter wavelengths are of considerable astrophysical interest. Several molecular transitions which are bright in star forming regions are polarized due to the magnetic fields associated with most stages of star formation (Vallée 2003). Lines may either be circularly polarized due to the Zeeman effect or linearly polarized through the Goldreich–Kylafis effect, or both. Line polarization is also known in late stages of stellar evolution where dense circumstellar shells often give rise to maser emission in millimeter lines (Menten 1996). At least in the case of SiO, the transitions may have very complex polarization characteristics due to magnetic fields and maser propagation.

The millimeter continuum may also be polarized in Galactic sources due to emission from non-spherical paramagnetic dust grains. The continuum radiation of extragalactic sources, notably the synchrotron emission from active galactic nuclei, is also often polarized. Its detection at millimeter wavelengths is of interest, since the lower optical depth allows us to look deeper into the sources than is possible at longer wavelengths and since these wavelengths are less affected by interstellar scattering.

The ideal polarimeter should therefore be capable of observing lines as well as continuum, and all four Stokes parameters should be measured. Given the usual weakness of the polarization signal in the millimeter range, a large telescope is advantageous if compact sources are to be measured. The few spectral polarization observations made previously at the IRAM 30m telescope measured circular polarization (Crutcher et al. 1996, 1999; Thum and Morris 1999). Linear polarization measurements were attempted in the continuum with

a bolometer (Lemke 1992). Many more observations of linear polarization were made at the James–Clark–Maxwell telescope (see Greaves et al. 2003, and references therein).

In October 1999 when we began developing XPOL, the IRAM 30m telescope had started a profound upgrade of its receivers. At the end of this transformation, the telescope was equipped with 4 single beam, dual polarization heterodyne receivers which cover most of the 75 to 270 GHz frequency range. All receivers have linearly polarized feed horns. Here we concentrate on work at 3mm wavelength with receivers A100 (vertically polarized) and B100 (horizontally polarized). The four Stokes parameters are derived from the IF signals from these receivers (the Intermediate Frequency is at 1.5 GHz) and refer to the right handed Nasmyth coordinate system  $\mathcal{K}_{\mathcal{N}}$  (Fig. 1) in which these receivers are stationary. In this configuration, the Stokes parameters relate to the time-averaged horizontal,  $E_x$ , and vertical,  $E_y$ , electric fields and their relative phase  $\delta$  (Born & Wolf 1975, chap. 10):

$$I = \langle E_x^2 \rangle + \langle E_y^2 \rangle \quad (1)$$

$$Q = \langle E_x^2 \rangle - \langle E_y^2 \rangle \quad (2)$$

$$U = 2 \langle E_x E_y \cos \delta \rangle \quad (3)$$

$$V = 2 \langle E_x E_y \sin \delta \rangle \quad (4)$$

This description of the Stokes parameters in terms of electric fields lends itself most naturally to our case where heterodyne receivers amplify the incoming electromagnetic fields. Stokes  $I$  and  $Q$  are thus obtained from power measurements, whereas Stokes  $U$  and  $V$  are measured as correlations. The fractional linear,  $p_L$ , and circular,  $p_C$ , polarization and the polarization angle,  $\tau$ , are then derived in the usual way.

Correlation polarimeters are well known in radio astronomy (Rohlfs & Wilson 2006, chapter 4.7). Heiles and collaborators (Heiles et al. 2001a,b; Heiles 2001c) give a very detailed description of this measurement technique as used at the Arecibo Observatory. To our knowledge, XPOL at the IRAM 30m telescope and its analog predecessor IFPOL (Thum et al. 2003) are the first such correlation polarimeters used at a large millimeter telescope.

## 2. Instrumental setup

The procedure which we designated XPOL, of cross correlation spectropolarimetry at the IRAM 30m telescope, makes use of existing observatory equipment as much as possible. Notably, we use the two single beam 3mm SIS receivers which are housed in separate dewars. This section describes the standard equipment inasmuch as relevant for polarization observations and the modifications made for XPOL.

## 2.1. Nasmyth optics

The 3mm receivers A 100 and B 100 located in the Nasmyth cabin view the subreflector through a series of optical elements shown very schematically in Fig. 1. We refer all polarization measurements to the coordinate system  $\mathcal{K}_N$  stationary in the Nasmyth cabin as shown in Fig. 1. Mirrors M3, M4, and M5 bring the incoming beam to the wire grid G3 which reflects vertical (parallel to the  $Y$ -axis of  $\mathcal{K}_N$ ) polarization to A 100 and transmits horizontal (parallel to  $X$ ) polarization to B 100. In the default setting, the wires of G3 are parallel to the plane of incidence. The Martin–Puplett interferometers (MPI) can be used to rotate the polarization direction for matching with the respective orientations of the 3mm and 1.3mm receivers (housed in the same dewars, but not shown here). The MPIs are located at the first beam waists. Additional optics, not shown, refocus the beams onto the receiver feed horns.

When mirror M5 is retracted from the beam, the receivers view M6 which focuses the beams onto the calibration unit which is equipped with the usual ambient and cold loads for the calibration of antenna temperature. A wire grid, G5, is employed for the calibration of the relative phase  $\delta$  (sect. 3.1).

## 2.2. Modifications for XPOL

The standard instrumental setup was modified in several respects for the polarization measurements. First, the local oscillator signal is normally derived from separate synthesizers (operating near 5 GHz and 100 MHz) for each receiver. In polarimetry, the two receivers share both the 5 GHz and the 100 MHz synthesizers. In this way, the phase noise between the two receivers is reduced to an acceptable level (see sect. 3.2).

The actual correlation between the two receiver signals is made in the spectral backend VESPA (VErsatile Spectroscopic and Polarimetric Analyzer) which is located in the observatory building and connected to the receivers in the Nasmyth cabin by circa 100m long coaxial cables. The length difference of these cables, originally found to be about 0.3m, gave rise to a very steep phase variation across the 500 MHz bandpass, the maximum bandpass available with the 3mm receivers. We adjusted the length of these cables until the global phase gradient was smaller than phase structure introduced by other components (Fig. 2). The residual difference of the electric paths is smaller than 5 cm. The detailed spectral behavior of the phase and its calibration is described below (sect. 3.1).

In non-polarimetric observations, the Martin–Puplett interferometers, MPI in Fig. 1, are tuned to a path difference which permits simultaneous maximum transmission of the 3

and 1.3mm frequencies observed<sup>1</sup>. The compromise setting implies a very small loss at each frequency. With XPOL we do not normally use the 1.3mm receivers in parallel with the 3mm receivers; although this operation mode is feasible, we tune the MPIs such that only the 3mm transmission is maximized, so that no losses occur.

The most profound modification was required for the spectral backend, which had to be capable of making cross correlations in addition to the autocorrelations, which are normally all that is needed on a single dish telescope. This substantial upgrade became practical after the Plateau de Bure (cross)correlator became available following the addition of a new antenna and new correlator to the IRAM interferometer. The integration of these components with the previous 30m correlator created a larger bandwidth correlator, dubbed VESPA (Paubert 2000). It is capable of simultaneously making the auto- and cross correlations required for the simultaneous measurement of the four Stokes parameters (eqns. 1 – 4). The data streams are organized such that auto- and cross correlations of each spectral subband are derived from the same digitizer, thus sharing the entire analog signal path. This greatly facilitates calibration (sect. 3.1). VESPA is an XF-type correlator which calculates the auto- and complex cross correlation functions and accumulates them during one observation phase (typically 2 sec in wobbler-switching), before their Fourier transforms are written on disk.

The VESPA hardware permits the following resolution/bandwidth combinations (in kHz/MHz) in polarimetry mode: 40/120, 80/240, 625/480<sup>2</sup>. The latter combination is the current optimum for continuum observations where the spectral channels are averaged to get one single power measurement for each Stokes parameter. The higher spectral resolution modes are used for line observations where the available bandwidth can, within limitations, be split into several sections at separate IF frequencies.

### 3. Calibration

Polarization observations as described above invoke the precise measurement of the four Stokes powers (eqns. 1–4) rather than just one measurement as in the usual total power observations. The Stokes  $I$  and  $Q$  powers are immediately derived from the vertically and horizontally polarized receivers A100 and B100 which are calibrated using the traditional hot/cold load technique (see, e.g. Downes (1988)). Calibration of the  $U$  and  $V$  powers

---

<sup>1</sup>Receivers at 1.3mm, A230 and B230, are housed in the same dewars as A100 and B100, but are not shown on Fig. 1.

<sup>2</sup>A further special mode is available with spectral resolution of 2.5 MHz and a bandpass of 960 MHz split into two 480 MHz subbands of identical IF coverage.

invoke new issues discussed in this section: the measurement of the relative phase between the receivers (sect. 3.1), decorrelation losses (sect. 3.2), and the signs of the Stokes parameters (sect. 3.3).

### 3.1. Calibration of phase

The phase  $\delta$  between the receivers A 100 and B 100 is derived for each spectral channel from the real and imaginary part of the cross correlation measured with VESPA. The intrinsic phase between orthogonally linearly polarized components of the incoming radiation field may be modified in many ways as the radiation passes down the signal chain. The most notable mechanisms potentially affecting  $\delta$  are *(i)* differences in the geometric paths through telescope and cabin optics up to the mixers, *(ii)* conversion of the electric field into voltages at the feed horns, *(iii)* amplification, filtering and transport of the signals downconverted to the first IF, *(iv)* transport in the long IF cables to the backend, and *(v)* downconversion to basebands in VESPA with the associated filtering and amplification. Stages *(i)* and *(ii)*, where the signals are at the radio frequency, are a priori the most likely ones to introduce differential phase shifts. A phase calibration unit is therefore best placed high up in the signal chain where it calibrates a maximum of these phase-affecting components.

#### 3.1.1. Method

Our method of phase calibration makes use of the hot/cold calibration unit located in the Nasmyth cabin (Fig. 1). Any phase shifts occurring at stage *(i)* in the complicated optical path between the receivers and M5 are therefore calibrated. Phase shifts picked up in front of M5 are however not calibrated. They manifest themselves as a component of the instrumental polarization which varies with elevation (sect. 5.5).

The phase calibration of XPOL consists of the 3 subscans of the standard temperature calibration (on sky, ambient load, and cold load) and an additional observation of the cold load (subscan No.4) where the wire grid G5 is introduced into the beam (Fig.1). The unpolarized hot-cold signal is thus converted into a strong linearly polarized signal which covers the entire bandwidth of the backend. The angle of the wires is fixed to  $53^\circ$ , which is close enough to  $45^\circ$  to transmit comparable power to both receivers, but distinct enough from  $45^\circ$  to avoid  $90^\circ$  ambiguities. The correct setting of this important angle was verified by temporarily introducing another wire grid G4 (Fig 1). At this location, the angle which the wires make with the horizontal plane can be precisely measured. This angle is  $54 \pm 0.5^\circ$ .

Its uncertainty represents the ultimate limit to the precision of XPOL polarization angle measurements.

From the 4 subscans of a phase calibration measurement the XPOL software calibrates the measured complex cross correlation spectrum in terms of antenna temperature. Fig. 2 shows amplitude and phase of such a phase calibration. VESPA is set to its broadest bandwidth (480 MHz) where calibration is most critical. In this mode, the bandpass is made up of 12 basebands generated by 12 image rejection mixers which are pumped by their respective LO3 local oscillators. The phase spectrum clearly shows this subband structure whereas the amplitude spectrum is smooth after calibration. The residual amplitude ripple which is due to reflections between the receivers and the cold load is of low relative amplitude and has no practical consequences (see sect. 3.1.2).

### 3.1.2. Precision

The phase spectrum consists of 3 components: an overall gradient across the bandpass, systematic offsets of each baseband, and an irregular phase bandpass for each baseband. The offsets are due to differences in the cable length of each of the twelve LO3. These differences could be made small or negligible, but they are inconsequential, since they can be precisely calibrated and they are stable in time due to the location of VESPA in an air-conditioned room. The same holds for the detailed shape of the phase bandpasses which are related to the individual filters and amplifiers for each baseband. No effort was therefore made to adjust their characteristics, since the signal-to-noise ratio available is clearly sufficient to allow rapid calibration of these effects on a channel-by-channel basis.

Line observations often use smaller bandwidths where fewer and different VESPA subbands are employed. Our phase calibration method works correctly for all VESPA polarimetry configurations (sect. 2.2). In particular, since the phase of each channel is measured, no assumptions are needed for the behavior of the phase across the receiver bandpass.

The small amplitude ripple ( $\sim 1\%$ ) of the phase calibration spectrum (Fig. 2) introduces a sinusoidal phase error of peak-peak amplitude  $\sim 0.6^\circ$ . This is a very small error which furthermore tends to cancel out in broadband (continuum) observations. The error might be detectable in spectral observations where the line is strongly linearly polarized. As this error exchanges power between Stokes  $U$  and  $V$ , it generates instrumental  $V$  at the level of  $0.01 \cdot U$  at the spectral channels near the maximum of the ripple amplitude and smaller elsewhere. The error is therefore negligible.

The overall gradient of the phase across the 500 MHz bandpass, due to a small residual

length difference of the IF cables, is of the order of the baseband offsets. This phase pattern is very stable, the (bandpass averaged) mean phase not usually varying by more than  $10^\circ$  during a night. Irregular phase jumps, like those expected from cable stress in the azimuth cable spiral or in the large elevation cable wrap, are not observed.

The only occasion when small phase jumps are seen is after the observing frequency has changed, e.g. when a new target source is observed. These phase changes are proportional to the frequency changes, and may be explained by small non-linearities in the frequency multiplication chain of the local oscillators. Phase variations due to changes in the telescope structure are small and have not been clearly detected (sect. 5.5).

### 3.2. Calibration of Stokes U and V spectra

Stokes  $U$  and  $V$  spectra are obtained from cross correlation of the two receivers (eqns. 3–4). The correlated power may therefore be affected by phase noise which is a well known issue for interferometers, but not normally of concern at single dish telescopes. If uncorrected, these losses introduce a systematic bias into the measurements of the linear and circular fractional polarization degrees and the polarization angle. We have used two methods to measure this loss which is proportional to the observing frequency. The first one uses a strongly polarized celestial source and is very time consuming. The second method exploits our new scheme of calibrating the relative phase. It therefore does not cost any extra observing time and its result is very precise. It is now routinely used by the XPOL calibration software.

#### 3.2.1. Celestial source

The field of view of a receiver in the Nasmyth focus is subjected to two rotations: *(i)* the parallactic rotation due to the alt-azimuth mount of the telescope, and *(ii)* the Nasmyth rotation about the elevation axis. Stokes  $Q$  and  $U$  of a linearly polarized celestial source therefore vary sinusoidally as the source is tracked. The amplitudes of the normalized sine waves,  $Q/I$  and  $U/I$ , must be the same and equal to the fractional linear polarization  $p_L$ . Decorrelation losses, however, make  $U$  smaller than  $Q$ , an easily observable effect on a strongly linearly polarized source.

We observed the SiO maser star  $\chi$  Cyg at 86.243 GHz (the  $v = 1, J = 2 \rightarrow 1$  transition) during 9 hours. The star’s position (declination  $\sim 33^\circ$ ) makes it culminate near the zenith, where more than a full period of the  $Q$  and  $U$  rotation is readily observed. The spectrum has



several features which are linearly polarized, as seen from the large difference in the spectra from the orthogonally polarized receivers (Fig. 3, top). We have obtained 58 such spectra per observing period from which we derived the sinusoidal variation of Stokes  $Q$  and  $U$  for each of the spectral channels. For the channels with sufficiently strong signal, we derive the maximum of the  $Q$  and  $U$  sine curves by least-squares fitting, and we plot them against each other. Fig. 3 (bottom) shows that the  $U$  amplitudes are systematically lower than the  $Q$  amplitudes by a factor  $1.20 \pm 0.01$ . This effect is constant during the five hours of the experiment, and we interpret it as a loss of  $U$  power due to decorrelation. The loss corresponds to an rms phase noise of 33 deg.

### 3.2.2. Using grid G5

In subscan 4 of the phase calibration measurement (sect. 3.1.1), the grid G5 is inserted into the beam. The cold load therefore radiates linearly polarized power into the receivers. Its  $Q$  and  $U$  components are determined from their power difference (eqn. 2) and from their correlation (eqn. 3), while total power is simply the sum of the powers (eqn. 1). For this fully linearly polarized signal, Stokes  $I$  and  $Q$  which are not affected by phase noise, can be used to predict  $U = \sqrt{I^2 - Q^2}$ . The difference between the measured and the predicted  $U$  is the decorrelation loss. From many measurements at 86.2 GHz we obtain a decorrelation loss of 14 %, in agreement with the loss derived from the  $\chi$  Cyg observation.

As a consistency check, we also calculate the Nasmyth (coordinate system  $\mathcal{K}_N$ ) polarization angle

$$\tau = \frac{1}{2} \arctan \left( \frac{U}{Q} \right) \quad (5)$$

using the measured  $Q$  and the loss-corrected  $U$ . We obtain  $54.4^\circ$  in agreement with the measurement on grid G4 (sect. 3.1). This good agreement verifies the implicit assumption that the circularly polarized power radiated by the polarized cold load is negligible ( $< 1\%$ ).

### 3.3. The signs of the Stokes parameters

The last peculiarity of polarization measurements is that contrary to Stokes  $I$  which is always positive, the other Stokes parameters can have any sign. While the determination of the sign of  $Q$  ( $= H - V$ ; eqn.2) is easily made by simply disconnecting one of the receivers, the calibration of the  $U$  and  $V$  signs is somewhat more involved.

### 3.3.1. Stokes $U$

Our preferred method for determining the sign of  $U$  is based on our knowledge of the sign of  $Q$  and knowing how to rotate an angle  $\tau$  measured in the righthanded system  $\mathcal{K}_N$  to the polarization angle  $\chi$  measured in the lefthanded  $(\alpha, \delta)$  system  $\mathcal{K}_*$  centered on a celestial target. The transformation involves an even number of reflections, one change of handedness, the Nasmyth rotation (anti-clockwise) about the elevation angle  $\epsilon$ , and a (clockwise) rotation by the parallactic angle  $\eta$ . This results in the relation

$$\tau = 90^\circ + \chi + \epsilon - \eta \tag{6}$$

The relation has been verified by observing linearly polarized sources of known position angle  $\chi$ , like the Crab Nebula (Wright & Foster 1980) and the moon (Thum et al. 2003). The Crab nebula is our primary angle (or  $U$ ) calibrator, since it is easily detected at the 30m telescope, it is strongly polarized, and its angle is well known ( $\chi = 155^\circ$ ) and rather constant across the face of the nebula (Wright & Foster 1980). An observation of the Crab Nebula is included in every polarimetry session at the 30m telescope, and it serves as a very powerful check of the stability of the XPOL data acquisition.

### 3.3.2. Stokes $V$

For Stokes  $V$  we adopt the IAU convention (IAU 1974):  $V = RHC - LHC$  where RHC (LHC) designate right (left) hand circular polarization. As usual, we take the electric vector of a RHC wave propagating toward the observer to describe a counterclockwise rotation. We determined the sign of  $V$  from 3 largely independent methods: *(i)* using first principles and checking them against the established usage of receivers in VLBI observations, *(ii)* converting unpolarized emission from a planet to circular of known sense with the help of a wire grid/quarterwave plate assembly, and *(iii)* converting the linearly polarized flux of the Crab nebula to circular of known sense with a quarterwave plate. These methods, described in detail in a separate note (Thum & Wiesemeyer 2005), give the same result, and the XPOL calibration software now gives the sign of  $V$  in agreement with the IAU convention.

## 4. Sensitivity

A polarimetric observation consists of a calibration of the antenna temperature and the phase, followed by a wobbler-switched observation of a target. A subsequent control measurement of the phase was soon abandoned because of the high stability of the phase in

the absence of large antenna motions or frequency changes. Fig. 4 obtained with the XPOL calibration package shows a typical observation of an Active Galactic Nucleus (AGN) from the list of the telescope’s pointing sources (*left*) and a spectral line observation (*right*). For the continuum observation, we used VESPA with a bandwidth of 480 MHz, close to the maximum IF bandwidth of the 3mm receivers. At this bandwidth, the channel spacing of 625 kHz generates  $\sim 700$  spectral channels. The XPOL software removes the instrumental phase from the phase of the target, derives the calibrated  $U$  and  $V$  spectra, and combines them with  $I$  and  $Q$  to give the spectra of  $p_L$ ,  $p_C$ , and the angle  $\chi$ . Their mean values obtained from averaging the spectral channels are given on the margin of the figure together with header information.<sup>3</sup>

Fig. 4 (left) illustrates the sensitivity obtainable in 3mm continuum observations. From the radiometer formula we expect an rms noise of 13 mK in 8 min of integration for one polarization (one receiver), given a system temperature of 200 K, a spectral channel spacing of 625 kHz, wobbler switching, and a backend efficiency of 87%. Since each Stokes spectrum combines the noise from two receivers, the noise of the Stokes spectra is expected to be  $\sqrt{2}$  larger, in agreement with our observation where we typically have an rms noise of 18 mK. The standard deviations of  $p_L$  and  $p_C$  are then derived for each spectral channel from error propagation. In continuum observations, the standard deviations are divided by the square root of the number of channels. We thus obtain a 0.33% formal rms error of the polarization degree and an rms uncertainty of  $1.2^\circ$  for the polarization angle.

The observation of 1308+326 discussed here was made during good weather with an optimized system in the context of a large 3mm polarization survey of AGNs (Thum et al., in preparation). The extent to which such data can be trusted depends on a good understanding of the systematic errors described in the next section.

## 5. Instrumental polarization

The many systematic effects which affect polarization observations are often collectively labelled instrumental polarization. In a rotationally symmetric antenna like the 30m telescope where ideally no instrumental polarization is expected (sect. 5.1), such systematic effects may occur due to subtle departures from symmetry or measurement problems. With the XPOL setup where correlation polarimetry directly measures the Stokes parameters, instrumental effects are conveniently classified according to the Stokes parameter affected. In the absence of calibration errors, power is not destroyed or created, but only exchanged

---

<sup>3</sup> At the observing frequency of 86 GHz the ratio  $S_\nu/T_A^* = 6.0$ .

between Stokes spectra. The most serious problems occur when total power is transported into other, usually much weaker Stokes parameters (sect. 5.2, sect. 5.3 and 5.4). Phase errors which exchange  $U$  and  $V$  power are negligible with XPOL due to its high level of phase stability (sect. 3.1.2). A subtle effect which may transport power between  $Q$  and  $U$  is described in sect. 5.5.

### 5.1. The perfect Cassegrain Telescope

For axisymmetrical telescopes such as center-fed paraboloids or Cassegrain telescopes no significant instrumental polarization can be induced by the optical system when suitably illuminated. This was shown for illumination by a Huygens source<sup>4</sup> in the optics approximation by Safak & Delogne (1976) and Hanfling (1970) and when diffraction is considered by Minnett & Thomas (1968) and Thomas (1976). In the latter case a balanced HE11 mode corrugated horn was shown to be an effective Huygens source with cross polarized sidelobes less than  $10^{-5}$  in amplitude for large telescopes ( $\geq 1000$  wavelengths) where any edge currents have negligible effect (see Ng et al. (2005) for a discussion of edge effects). The electric field in the telescope aperture plane is then everywhere parallel and no cross-polarization can thus exist in the far field no matter what asymmetries may exist in the illumination or phase distribution. Thus the far field polarization will be determined by the polarization of the effective field distribution which illuminates the subreflector from the secondary focus.

### 5.2. Feed imperfections

The feed horn is the receiver component first encountered by the incoming radiation. Imperfections of feedhorns may give rise to cross-polarization which then propagates down the rest of the signal chain. The problem which may easily reach the 10% level is well known in radio astronomy (Conway & Kronberg 1969). Even in modern radio interferometers, cross-polarization arising from the feeds (the “D-terms” of the interferometer response) is typically at the level a few percent (Cotton 1999). Turlo et al. (1985) describe the linear polarization characteristics of a 6cm receiver at the Effelsberg 100m telescope.

Cross-polarization in the 30m receivers may be expected to be less serious than in these cases. For example, in XPOL, the two linear polarizations are detected by separate receivers,

---

<sup>4</sup>In this context a “Huygens source” is one for which the  $\mathbf{E}$  and  $\mathbf{H}$  fields are related as for a plane wave in free space.

each employing a circular corrugated horn followed by a rectangular mono-mode waveguide which suppresses the cross polarized field. An even stronger reduction of the cross-polar component occurs at the grid G3 (Fig. 1). We tried to measure the residual cross-polarization by introducing additional wire grids right in front of the entrance windows of the receiver dewars. No signal was detected when looking at the hot/cold loads with the wire grids orthogonal to the nominal polarizations of the receivers. We derive a relatively imprecise upper limits of  $\leq 3\%$  for the on-axis feed cross-polarization. More sensitive astronomical measurements are described below.

### 5.3. On-axis polarization

In a more precise study of the instrumental polarization, we looked at the false polarization signal from unpolarized and strong sources. In the course of the AGN survey, many such observations were made on planets and HII-regions. Fig. 5 shows the values obtained, their mean values and variances are given in Table 1. The data represent the on-axis instrumental polarization which is relevant for observation of point sources.

The values and their variances are drastically different for these 3 (non- $I$ ) Stokes parameters. We note that this pattern stayed approximately constant during the 2 weeks of the AGN survey, and it was also found to be the same at subsequent polarimetry sessions. The large variance of  $Q_i$  is clearly due to temporal variations of the atmospheric emission. This was verified by omitting all observations made under unstable conditions, including many made through cumulus clouds. Retaining only the observations obtained under stable conditions, the variance of  $Q_i$  approaches that of  $U_i$ , but always remains some 10 to 30% higher. We attribute this persistent difference to our way of measuring the two parameters:  $Q$  is derived from power measurements, whereas  $U$  is derived from their correlation. Fluctuations of receiver gain or atmospheric emission which are faster than the wobbler frequency are therefore suppressed in  $U$ , but not in  $Q$ .

By far the best performance is obtained in  $V$ , where the variance approaches the scatter expected from system noise, and the mean instrumental offset  $V_i$  is negligibly small. Circular polarization of point sources can therefore be observed without any corrections for instrumental polarization. This is even true for extended sources after the improvements described in sect. 5.4.

Despite Stokes  $V$  and  $U$  being both derived from correlations, their variances are clearly not the same. We attribute the higher variance in  $U$  to small intrinsic linear polarization of the supposedly unpolarized sources. A few sources with  $p_L \lesssim 1\%$ , possibly among the

compact HII–regions in this sample (Glenn et al. 1999), are sufficient to increase the sample variance to the observed value.

Observations of linear polarization need a stable atmosphere, and the instrumental polarization must be subtracted from the observed Stokes  $Q$  and  $U$  values. These systematic effects set in at  $p_L \lesssim 1.5\%$  and must be carefully checked.

#### 5.4. Beam maps

In an effort to understand the origin of the instrumental polarization observed on–axis (sect. 5.3), we have made beam maps in the four Stokes parameters. These maps were observed in the on–the–fly mode without any switching. Reference fields were observed before each subscan in order to calibrate the receiver gain. The brightest planets which had diameters smaller than the main beam were mapped. Fig. 6 shows the  $Q$ ,  $U$  and  $V$  maps obtained at two epochs: in 1999 when our polarimetry tests started (left), and in 2005 (right) obtained in the context of the AGN survey mentioned in the previous section after the changes described below were made.

The 1999  $Q$  and  $V$  maps are characterised by strong bipolar patterns reaching amplitudes larger than  $\pm 2\%$ . The patterns are mostly antisymmetric about the  $y$ –direction which is the vertical in the Nasmyth cabin. Maps taken at different elevation and azimuth, and therefore different relative orientations of the systems  $\mathcal{K}_*$  and  $\mathcal{K}_N$ , invariably confirm this antisymmetry about the  $y$ –direction. The bulk of the polarized sidelobe power therefore arises in components stationary in the Nasmyth cabin.

The intersection of the  $x$  and  $y$ –arrows is the pointing direction of the telescope. The  $Q$  map therefore suggests that the two receivers were misaligned, mainly along the horizontal axis. The amplitudes of the positive and negative lobes correspond to an angular offset of  $\sim 1.0''$  which is the typical precision to which receivers can normally be aligned.

Cross–talk between the IF signals was also investigated as a possible cause of the instrumental polarization. Injecting a strong signal at various points of the IF chain of one receiver, the response was measured in the IF of the other receiver and found to be better than  $-40$  dB.

In 2005 we succeeded in aligning receivers A 100 and B 100 using a more accurate method which minimized the instantaneous difference signal from the receivers. A precision of the alignment of  $0.3''$  or better was reached; this is difficult to improve upon with heavy receivers mounted in mechanically independent dewars (Nasmyth image scale:  $0.7''/\text{mm}$ ).

Another improvement was the orientation of the wire grid G3 (Fig. 1). In the default setting of the 30m Nasmyth optics, this grid must have its wires parallel to the plane of incidence. When a grid is used in a divergent beam (like in the case of G3), this orientation is however not optimum with respect to cross polarization. Chu et al. (1975) have shown that in this case the wires should be perpendicular to the plane of incidence if enhanced cross polarized sidelobes are to be avoided (about -24 dB in their case). In the appendix (sect. A) we describe in detail how imperfections of the grid and its orientation introduce cross polarization, and we demonstrate quantitatively that the polarization pattern observed with well-aligned receivers is fully explained by the wrongly oriented G3. Most of the data of the AGN survey, however, were obtained with the grid G3 in its optimum position.

The 2005 maps show the combined effects of the optimum alignment and the correctly oriented G3. Striking improvements were obtained in  $Q$  and  $V$ , and a general trend from mostly bipolar to mostly quadrupolar is observed in all 3 maps. With the possible exception of  $Q$ , the beam patterns are no longer dominated by misalignment. This quadrupolar polarization pattern is exactly what is expected in a Cassegrain antenna (Olver et al. 1994) whose optical layout is symmetric about the radio axis and which is illuminated by a feed with a  $m = 2$  polarization component (see Appendix A.2). The polarization sidelobes observed in 2005 are thus likely to come mostly from non-circularity of the feeds' electrical characteristics.

The values measured at the intersection of the  $x$  and  $y$ -axis, i.e. the pointing direction of the telescope, are the on-axis instrumental polarizations  $Q_i$ ,  $U_i$ , and  $V_i$  discussed above (sect. 5.3). Although the observations of the unpolarized point sources (Tab. 1) and the maps were not made contemporaneously, the agreement between the two sets of values for the instrumental polarization is remarkably good. In the center of the  $Q$  map, there is a large slope where angle-of-arrival fluctuations can induce random  $Q_i$  values. This is not the case for  $U$ . This difference may help to explain why we find the variance of  $Q_i$  to be always larger than that in  $U_i$ , even under good atmospheric conditions.

### 5.5. Gain variation with elevation

The IRAM 30m telescope has a homologous design which is optimized for an elevation of  $43^\circ$ . The residual surface errors introduce a degradation of the on-axis gain of the antenna, or its aperture efficiency  $\eta_a$ , when moving away from the design elevation. Greve et al. (1998) showed that at  $\lambda 3\text{mm}$   $\eta_a$  decreases by about 4 – 5% at the extreme elevations relative to its optimum value near the design elevation.

Given this marked dependence of  $\eta_a$  on elevation, we suspect that the residual deformations of the structure may be slightly asymmetric in the vertical and horizontal directions. This would give rise to instrumental polarization, primarily in  $Q$  when observed in the horizontal system. The receivers see this polarization after the Nasmyth rotation as a mixture of  $Q$  and  $U$  which has a well-defined elevation dependence. We have therefore re-analysed the instrumental polarization data presented in sect. 5.3, but we do not find any dependence on elevation stronger than 1.5%. The precision of this upper limit is however strongly limited by the heterogeneity of the data and by the incomplete coverage of the elevation range.

A new opportunity for a more precise measurement of this effect occurred in May 2005 when the quasar 3C454.3 had an outburst. We made 45 dedicated XPOL measurements over the elevation range from  $10^\circ$  to  $69^\circ$ . Due to the brightness of the source ( $S_\nu \simeq 15$  Jy) the precision of an individual polarization measurement was  $\lesssim 0.1\%$ , and the linear polarization of the quasar ( $p_L = 4\%$ ,  $\chi = 60^\circ$ ) was easily detected. The suspected elevation dependence of the instrumental polarization would show up as an elevation modulation of  $p_L$  around its mean value. Indeed such modulations were found at levels of 1.5% ( $Q$ ) and 0.5% ( $U$ ). Unfortunately, these modulations are indistinguishable from short-timescale intrinsic polarization variations of the quasar. Indeed, our measurements show that the total power (Stokes  $I$ ) of the quasar varied over the 12 hours monitoring period by more than 20%. We therefore take these quasar measurements only to confirm our previous upper limit of 1.5% for any polarization-dependent gain variation with elevation.

## 6. Conclusions

XPOL, the first correlation polarimeter on a large single dish millimeter telescope, is a versatile instrument, capable of measuring line and continuum in all four Stokes parameters simultaneously. The setup makes use of the Observatory's 3mm (single pixel) heterodyne receivers which are housed in separate dewars on mechanically independent mounts. Our study shows that these receivers and their arrangement, which were not designed with polarization observations in mind, can nevertheless be used efficiently for many types of polarization observations.

In particular, all issues related to calibration were solved satisfactorily. The instrumental phase is precisely measured ( $\lesssim 1^\circ$ ) for all spectral channels individually, and it is very stable in time. A new method is applied for precisely measuring the decorrelation losses.

The many facets of instrumental polarization, in practice the factors limiting the precision of XPOL observations, were studied at 3mm wavelength for all Stokes parameters



in much detail. The most information can be drawn from maps of the Stokes beams. We showed that the pattern and strength of the polarization sidelobes very sensitively depends on the precision of the alignment between the receivers. Only when a precision of  $\lesssim 0.3''$  was reached, did we see the 4-lobed pattern expected in a Cassegrain telescope with its symmetry about the radio axis. This symmetry does not appear to be destroyed by additional reflections on the flat mirrors of our Nasmyth focus. The 4-lobed structure of the polarization sidelobes and their maxima are then determined by slight differences in the electric parameter (polarization, beam width, etc.) of the feedhorns.

The practical limits for XPOL observations of point sources can be inferred from the values in Stokes  $Q$ ,  $U$  and  $V$  at the center of the Stokes maps. These values are compatible with the “false polarization” measured on strong and unpolarized point sources. We conclude that Stokes  $Q$ , which is measured as a power difference, is most affected by instrumental polarization, whereas Stokes  $U$  and  $V$ , which are measured as cross correlations, are very little affected. The lower instrumental polarization of  $U$  and  $V$  is due to the insensitivity of correlations to fluctuations of receiver gain and atmospheric emission. An additional disadvantage arises for  $Q$  under an unstable atmosphere where the wobbling period may be too long for complete cancellation of the emission fluctuations.

In summary, XPOL observations of Stokes  $U$  and  $V$  are possible down to the  $\sim 0.5\%$  level before systematic effects set in, both for point-like and extended sources. Instrumental polarization limits Stokes  $Q$  observations at the 1.5% level. With proper precaution, this limitation can be overcome for point sources. Measurements of the linear polarization of extended sources are the most difficult observations with XPOL.

The design of a new receiver optimized for polarization would have to pay special attention to the feed, as its cross polarization constitutes the ultimate limit for systematic measurement errors. The alignment of the two feed horns, the next largest source of systematic error, appears easier if the feed horns (and the subsequent radiofrequency components) are housed in the same dewar, or even better, only one feed is used for the two polarizations. It therefore appears quite feasible on a big single dish millimeter telescope for a carefully designed polarization receiver to keep instrumental polarization well below the 0.5% level.

We wish to acknowledge the unfailing support by Manuel Ruiz and his team of telescope operators during the long and sometimes strenuous commissioning of XPOL. M. Torres (IRAM) helped through frequent discussions and by building a phase shifter used in an initial analog version of XPOL. The support by the IRAM backend group was essential in the construction of the VESPA backend, including its capability of making cross correlations. We also thank M. Carter (IRAM) for discussions and help.

## A. Instrumental polarization generated in a wire grid

In the optical setup of the XPOL polarimeter, the wire grid G3 (Fig. 1) has an important function, since it is used to split the incoming radiation into its vertical and horizontal components which are subsequently recorded by receivers A100 and B100. Any imperfections of G3 generate cross polarization which may be recorded as instrumental polarization. We therefore studied the polarization performance of wire grids in some detail, both when illuminated by parallel beams (sect. A.1) and by divergent beams (sect. A.2).

### A.1. Grid in a parallel beam

The bandwidth of a wire grid is potentially very large, the upper frequency of operation being determined by the intrinsic accuracy with which the grid can be made, and perhaps by the limited conductivity of the wires. However at millimeter wavelengths, we are close to these limits, and the splitter grid G3 and also the other grids in the receiving system, have only a finite discrimination against the unwanted linear polarization. There is first of all the intrinsic discrimination for a perfect grid, and secondly that due to errors in manufacture which render the grids non-ideal. Both effects have been studied by Houde et al. (2001).

One polarization is selected by reflection, when the discrimination is measured by the reflection coefficient for polarization perpendicular to the wires  $R_{\perp}$ . The orthogonal polarization is selected by transmission when the transmission coefficient  $T_{\parallel}$  for parallel polarization is appropriate. From the equations 59, 60, 66 and 67 of Houde et al. (2001) the amplitude reflection (R) and transmission (T) coefficients are for plane wave illumination

$$R_{\perp} = -i(1 - \alpha^2)x/\gamma \tag{A1}$$

$$R_{\parallel} = -(1 - i2\gamma Dz)/(1 + (2\gamma Dz)^2) \tag{A2}$$

$$T_{\parallel} = 1 + R_{\parallel} \tag{A3}$$

$$T_{\perp} = 1 - R_{\perp} \tag{A4}$$

where for the splitter,  $\gamma = 1/\sqrt{2}$ , the wire's radius is  $a$ , their separation is  $d$ , and  $x = \pi^2 a^2/\lambda d$ ,  $z = \log_e(\frac{d}{2\pi a})$  and  $D = \frac{d}{\lambda}$ . For the (favorable) case where the grid is rotated  $45^\circ$  around an axis parallel to the wires  $\alpha = \frac{1}{\sqrt{2}}$  otherwise  $\alpha = 0$ .

The response of a complex cross correlator to unpolarized radiation with components  $e_{\parallel}$ ,  $e_{\perp}$  is

$$\Gamma = e_{\parallel}^2 R_{\parallel} T_{\parallel}^* + e_{\perp}^2 R_{\perp} T_{\perp}^*$$

which can be expressed as components of the Mueller matrix (Tinbergen 1996; Heiles 2001c) as

$$M_{IU} + iM_{IV} = \frac{I}{2}[R_{\parallel}(1 + R_{\parallel}^*) + R_{\perp}(1 - R_{\perp}^*)]$$

For  $d = 0.1\text{mm}$ ,  $a = 0.0125\text{mm}$  and frequency 86 GHz, such as used with XPOL, eqs. A1–A4 yield  $R_{\perp} = -ix = -i 0.0034$ ,  $R_{\parallel} = -1 + i 0.00976$ ,  $T_{\perp} = 1 + i 0.0034$ ,  $T_{\parallel} = -i 0.00976$  and thus

$$\frac{M_{IU} + iM_{IV}}{I} = 0.000053 + i 0.0032 \quad (\text{A5})$$

The effects of random errors in the spacing of the wires may lead to larger values for  $T_{\parallel}$  (and perhaps  $R_{\perp}$  also). Houde et al. (2001) give some representative values for transmittance  $T_{\parallel}^2$  in their Figure 3, ( $a = 0.0125\text{mm}$ ). An approximate interpolation and scaling to the frequency of the XPOL splitter G3 give  $T_{\parallel}^2 = 1.8\%$  for a 5% error in spacing, and  $T_{\parallel}^2 = 3.2\%$  for a 16% error. Thus the polarization splitter grid should give a polarization discrimination of at best 0.3% (eq. A5). More realistically it is perhaps 2–3%, when up to 16% construction errors are considered.

The H and V optical branches between the polarization grid and the correlator will however provide further polarization discrimination due to additional grids and the receiver horns. Even if this additional rejection amounts to only 5% cross polarization, the overall cross polarization expected for the system would be at most 0.1%. So the initially measured values of the order of up to 2% cross polarized sidelobes are unexpected.

## A.2. Grids in a divergent beam

Grids such as that used in the polarization splitter are very good at "cleaning up" the linear polarization of a parallel beam. However in a divergent beam, as in the Pico Veleta receiving system, they can give rise to quite significant cross polarization. This was shown both experimentally, and theoretically, by Chu et al. (1975). They show (see their eqs. 9 and 10) that the electric fields parallel and perpendicular to the wires are as follows:

$$E_{\parallel} = -E_{in}\cos(\beta)[1 - \sin^2(\phi)(1 - \cos(\theta) - \sin(\theta)\sin(\phi)\cot(\gamma))] \quad (\text{A6})$$

$$E_{\perp} = -E_{in}\cos(\beta)[\sin(\phi)\cos(\phi)(1 - \cos(\theta)) + \sin(\theta)\sin(\phi)\cot(\gamma)] \quad (\text{A7})$$

Here  $\beta$  is the inclination of the grid to the beam axis ( $45^\circ$ ),  $\theta$  and  $\phi$  define directions relative the beam axis, and  $\gamma$  specifies the orientation of the wires in the plane of the grid. If the wires are perpendicular to the incident beam axis (perpendicular to the plane of incidence), then

$\cot(\gamma) = 0$  and only a minimal second-order cross-polarization is present. However for the alternative orientation of the wires  $\cot(\gamma) = 1$ , a large first-order cross-polarization is present after the beam reflects from the grid. The first-order cross-polarization is proportional to the sin of the angle  $\theta$  relative to the beam axis, and has a  $m = 1$  variation around the beam axis ( $\cos(\phi)$ ). This dipolar ( $m = 1$ ) symmetry agrees with that observed for  $M_{IU}$  and  $M_{IV}$  (Fig. 6, left column). Furthermore, since at the 30m telescope  $\theta$  reaches about  $3^\circ$ , it seems possible to generate a few percent of instrumental polarization by this mechanism.

We estimate the magnitude of the cross-polarization from a model of the electric field distributions  $\mathbf{E}_A(\mathbf{x}, \mathbf{y})$ ,  $\mathbf{E}_B(\mathbf{x}, \mathbf{y})$  in the telescope aperture associated with receivers A100 and B100. The fields are calculated using equations A6 and A7. The effects of differential pointing errors and defocus can be simulated by the addition of linear or quadratic phase terms. Identical Gaussian tapers have been assumed, but of course other tapers and field distributions can be accommodated. The corresponding far field radiation patterns calculated by Fourier Transform are then  $\mathbf{A}(\theta, \phi)$ , and  $\mathbf{B}(\theta, \phi)$ . The inputs to the correlator, when the telescope is illuminated by unpolarized radiation with (uncorrelated) components  $e_\times, e_{co}$  from the direction  $\theta, \phi$  are

$$\begin{aligned} V_a &= e_\times A_\times(\theta, \phi) + e_{co} A_{co}(\theta, \phi) \\ V_b &= e_\times B_{co}(\theta, \phi + \frac{\pi}{2}) - e_{co} B_\times(\theta, \phi + \frac{\pi}{2}) \end{aligned}$$

from which we derive the relevant components of the corresponding Mueller matrix as:

$$\begin{aligned} I(\theta, \phi) &= \langle V_a^2 \rangle + \langle V_b^2 \rangle \\ M_{IQ}(\theta, \phi) &= \langle V_a^2 \rangle - \langle V_b^2 \rangle \\ M_{IU}(\theta, \phi) + i M_{IV}(\theta, \phi) &= \langle V_a V_b^* \rangle \\ &= \frac{I}{2} [A_\times(\theta, \phi) B_{co}^*(\theta, \phi + \frac{\pi}{2}) - A_{co}(\theta, \phi) B_\times^*(\theta, \phi + \frac{\pi}{2})] \end{aligned}$$

Here we have taken the two beams to be rotated (about their axes by  $90^\circ$ ) to have orthogonal linear polarization.

Any periodicity of  $M_{IU}(\theta, \phi)$  or  $M_{IV}(\theta, \phi)$  in the angle  $\phi$  about their axes will be essentially determined by that of the cross-polarized beams  $B_\times$ , since the co-polarized beams will to a first approximation be invariant with  $\phi$ . The far field beams are just rescaled and smoothed images of the secondary focus field distribution in amplitude and polarization, provided that this field distribution radiates as a Huygens source. Then the far field will have also the same periodicity. That is, when expressed as series in  $\cos(m\phi)$ ,  $\sin(m\phi)$  they will have the same  $m$  values. In the present case where the effective source at the secondary focus is approximately that of the beam waist of a Gaussian beam, the assumption of a Huygens source may be justified.

Many imperfections in the optical system leading to cross polarization might be expected to correspond to higher order modes of circular waveguides. For example corrugated waveguides operating off the design frequency would radiate an excess of the  $TE_{11}$  or  $TH_{11}$  mode, both of which have an  $m$  value, as defined above, of 2. The only modes with  $m = 1$  are  $TE_{01}(H_{01})$  and  $TH_{01}(E_{01})$ , neither of which radiate along the beam axis and which are very difficult to excite. An exception is provided by an offset elliptical mirror which gives a field distribution with a fan like divergence of field lines across the beam — with a large  $m = 1$  component (Murphy 1987). In a similar way, the polarization splitter grid can induce such cross polarization when used at a non-optimum orientation ( $\cot \gamma = 1$ ). A similar  $m = 1$  asymmetry could result from a lateral displacement in the telescope aperture of a  $m = 2$  cross-polarized electric field pattern.

Fig. 7 illustrates the roles of the polarization splitter and receiver misalignment. It displays the results from three simple models. The far field radiation patterns for each receiver (A and B) were calculated by Fourier Transform of corresponding electric field distributions in the aperture plane. The equations of Chu et al. (1975) were used to describe their polarization and linear phase gradients were applied to simulate pointing offsets. A Gaussian illumination (14 dB taper) was assumed. The lefthand column of Fig. 7 has  $M_{IQ}$ ,  $M_{IU}$ ,  $M_{IV}$  for the case of 0.8 arc seconds offsets between receivers A 100 and B 100, and for optimum orientation of the polarization splitter. The  $M_{IV}$  values are in this case zero within the rounding errors of calculation. The middle column has results for non-optimum orientation and no misalignment. The righthand column includes in addition a pointing offset of 0.8 arc seconds between the two receivers. The overall similarity between the latter model maps and the maps of Fig. 6 (left column) demonstrates that both effects, an alignment error and a wrong orientation of the splitter G3, are needed to explain the 1999 maps.

Since the polarimeter is essentially a zero spacing interferometer, many of the above considerations will apply also to interferometers with spaced antennas.

## REFERENCES

- Born, M. & Wolf 1975, “Principles of Optics”, 5<sup>th</sup> edition, Pergamon Press, London
- Chu, T.S., Gans, M.J., & Legg, W.E. 1975, The Bell System Technical Journal, vol. 54, 1665
- Conway, R.G. & Kronberg P.P. 1969, MNRAS,142, 11
- Cotton, W.D. 1999, in “Synthesis Imaging in Radio Astronomy II”, Eds. Taylor, Carilli, and Perley, ASP: San Francisco, Conf. Ser. 180

- Crutcher, R. M., Troland, T. H., Lazareff, B., Paubert, G., & Kazès, I. 1999, *ApJ*, 514, L121
- Crutcher, R. M., Troland, T. H., Lazareff, B., & Kazes, I. 1996, *ApJ*, 456, 217
- Downes, D. 1988, in “Evolution of Galaxies and Astronomical Observations”, ed. I. Appenzeller et al., *Lec. Notes in Phys.* 333, Springer Verlag, Heidelberg, p. 351
- Glenn, J., Walker, C.K., Young, E.T. 1999, *ApJ*, 511, 812 – 821
- Greaves, J.S., Holland, W.S., Jenness, T., Chrysostomou, A. Berry, D.S., Murray, A.G., Tamura, M., Robson, E.I., Ade, P.A.R., Nartallo, R., Stevens, J.A., Momose, M., Morino, J.-I., Moriarty-Schieven, G., Gannaway, F., Haynes, C.V. 2003 *MNRAS*, 340, 353 — 361
- Greve, A., Neri, R., & Sievers, A. 1998, *A&AS*, 132, 413
- Hanfling, J.D. 1970, *I.E.E.E. Trans. Antennas and Prop.*, AP18, 192—196
- Heiles, C., et al. 2001, *PASP*, 113, 1274
- Heiles, C., et al. 2001, *PASP*, 113, 1247
- Heiles, C. 2001, *PASP*, 113, 1243
- Houde, M., Akeson, R.L., Carlstrom, J.E., Lamb, J.W., Schleuning, D.A., Woody, D.P. 2001, *PASP*, 113, 622 – 623
- IAU 1974, *Transactions of the IAU vol.15B*, p.166 (1073)
- Lemke R. 1992, PhD thesis, University of Bonn
- Menten, K. M. 1996, Masers at mm and submm wavelengths, in “Science with large mm arrays”, Ed. P.A. Shaver, *Proc. of the ESO-IRAM-NFRA-Onsala workshop*, Springer: Berlin
- Minnett, H.C. and Thomas, B. *MacA.* 1968, *Proc. I.E.E.* 115, 1419 – 1430
- Murphy, J.A., 1987, *Int. J. Infrared and Millimeter Waves*, vol. 8, 1165
- Ng, T., Landecker, T.L., Cazzolato, F., Routledge, D., Gray, A.D., Reid, R.I., and Veidt, B.G. 2005, *Radio Science*, Volume 40, Issue 5, CiteID RS5014
- Olver, A.D., Clarricots, P.J.B., Kishk, A.A., and Shafai, L. 1994, *Microwave horns and feeds*, *IEEE Electromagnetic wave series* 39

- Paubert, G. 2000, IRAM report
- Rohlfs, K. & Wilson, T.L. 2006, “Tools of Radio Astronomy”, 4<sup>th</sup> edition chapter 3, Springer Verlag
- Safak, M. and Delogne, P.P. 1976, I.E.E.E. Trans. Antennas and Prop., **AP-24**, 497 – 501
- Tinbergen, J. 1996, Astronomical Polarimetry, Cambridge University Press
- Thomas, B. MacA. 1976, Electron. Lett., **12**, 218 – 219
- Thum, C. and Morris, D. 1999, A&A, 344, 923 – 929
- Thum, C., Wiesemeyer, H., Morris, D., Navarro, S., and Torres M. 2003, SPIE vol. 4843, 272 – 283
- Thum, C. & Wiesemeyer, H. 2005,  
<http://www.iram.fr/~thum/stokesV/wpage/wpage.html>
- Turlo, Z., Forkert, T., Sieber, W., and Wilson W. 1985, Astron.Atrophys. 142, 181–188
- Vallée, J. P. 2003, New Astronomy Reviews 47, 85 – 168
- Wiesemeyer, H., Thum, C., and Walmsley, C. M. 2004, A&A, 428, 479
- Wright, M.C.H. & Forster, J.R. 1980, ApJ, 239, 873

Table 1: On-axis instrumental polarization, in percent.

---

$Q_i$	=	0.76	±	1.33
$U_i$	=	-0.26	±	0.37
$V_i$	=	-0.03	±	0.12

---



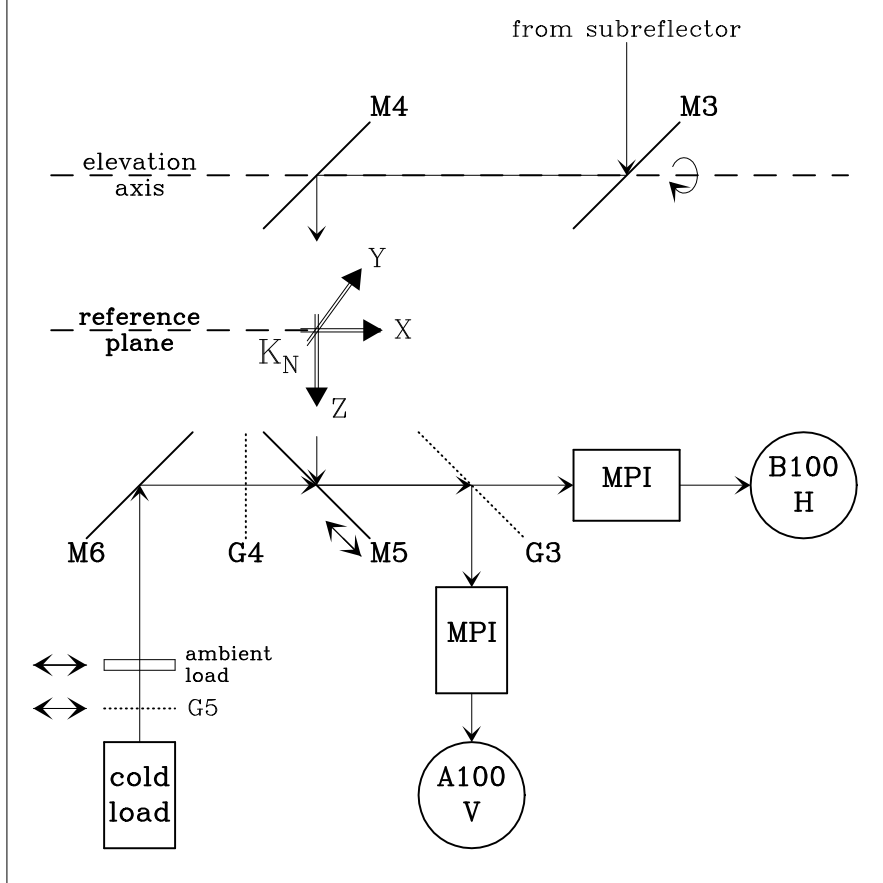


Fig. 1.— Schematic of the optical paths in the Nasmyth cabin of the 30m telescope. Radiation coming down from the subreflector is relayed by several mirrors, of which M3 rotates about the elevation axis, to the wire grid G3 which reflects vertically linearly polarized power to the 3mm receiver A100 and transmits horizontal power to B100. The first beam waist is located at the Martin–Puplett interferometers, MPI. When mirror M5 is retracted from the beam, as indicated by the  $\longleftrightarrow$  symbol, both receivers look at mirror M6 which focuses their beams onto the calibration unit. Wire grid G4 is occasionally inserted for calibration of the orientation of G5 (see sect. 3.1.1). We define the polarization parameters in the righthanded coordinate system  $\mathcal{K}_N$ , stationary in the Nasmyth cabin and located at the reference plane where  $X$  is transverse horizontal,  $Y$  is vertical (pointing upward), and  $Z$  points in the direction of beam propagation.

CAL PHASE SIO(V1;J:2-1 scan 9261 1-JUL-2005  
 UT: 12:16:52.64 LST: 6:42:2.68 HA = 6.701  $\varepsilon = 62.1^\circ$   $\eta = 90^\circ$   $\chi_0 = 62.1^\circ$   
 $T_{\text{sys}} = 89$  K  $t_{\text{int}} = 0.3$  min file: /project/thum/ifpol/055-05/spectra.30m

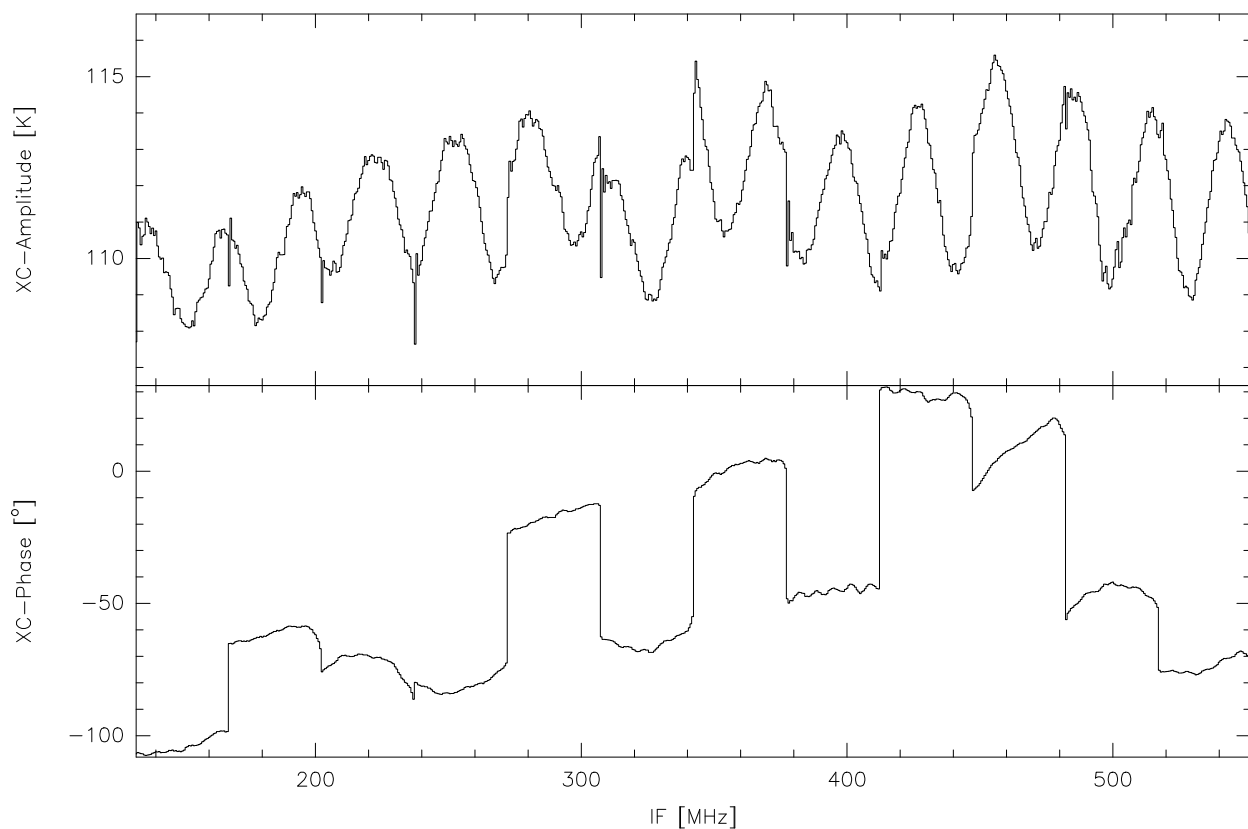


Fig. 2.— Phase calibration with VESPA in broadband mode. The 480 MHz global bandpass is split up into 12 basebands which have distinctly individual bandpass characteristics. For each of the 765 spectral channels the amplitude (*upper panel*) and phase (*lower panel*) is derived with precisions of  $\leq 1\%$  and  $\leq 1^\circ$ , respectively, except for a few channels at subband edges. The inconsequential standing wave of period 29.1 MHz in the amplitude spectrum (see sect. 3.1.2) arises from reflections between the receiver and the calibration unit separated by 5.1 m.

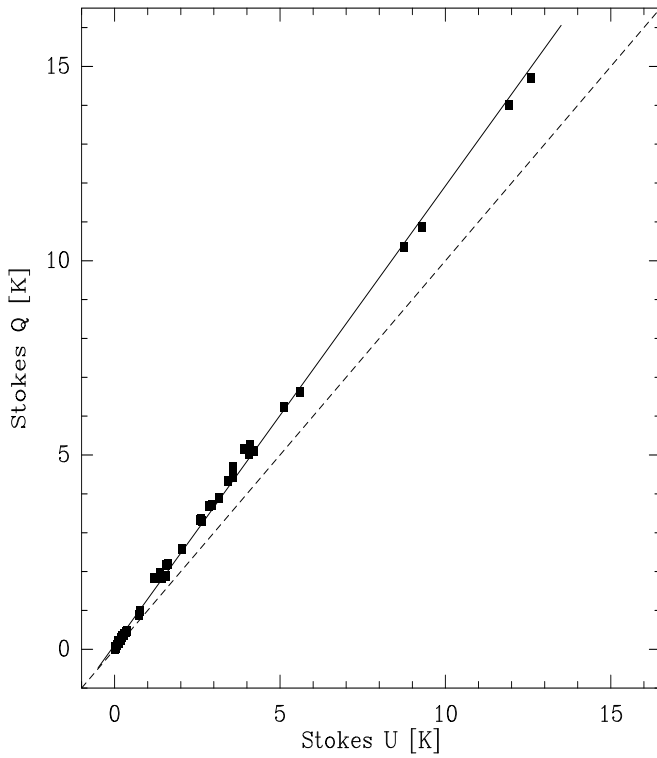
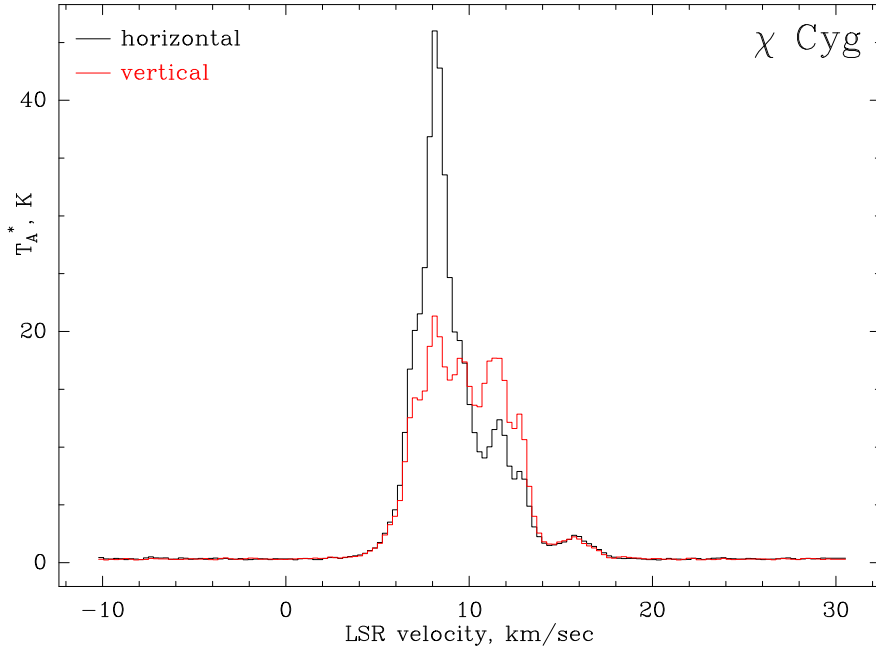


Fig. 3.— Measurement of the correlation loss using the strongly polarized 86.243 GHz SiO emission from the star  $\chi$  Cyg. *top*: 58 observations like the one shown here were made, during which the Nasmyth polarization angle  $\tau$  rotated by more than one period. *bottom*: The resulting amplitude, as measured in the Nasmyth system  $\mathcal{K}_N$ , of the  $U$  sine wave is smaller than that of  $Q$  for all channels as indicated by the departure from the  $45^\circ$  line (dashed). The systematic difference is ascribed to decorrelation losses in  $U$ .

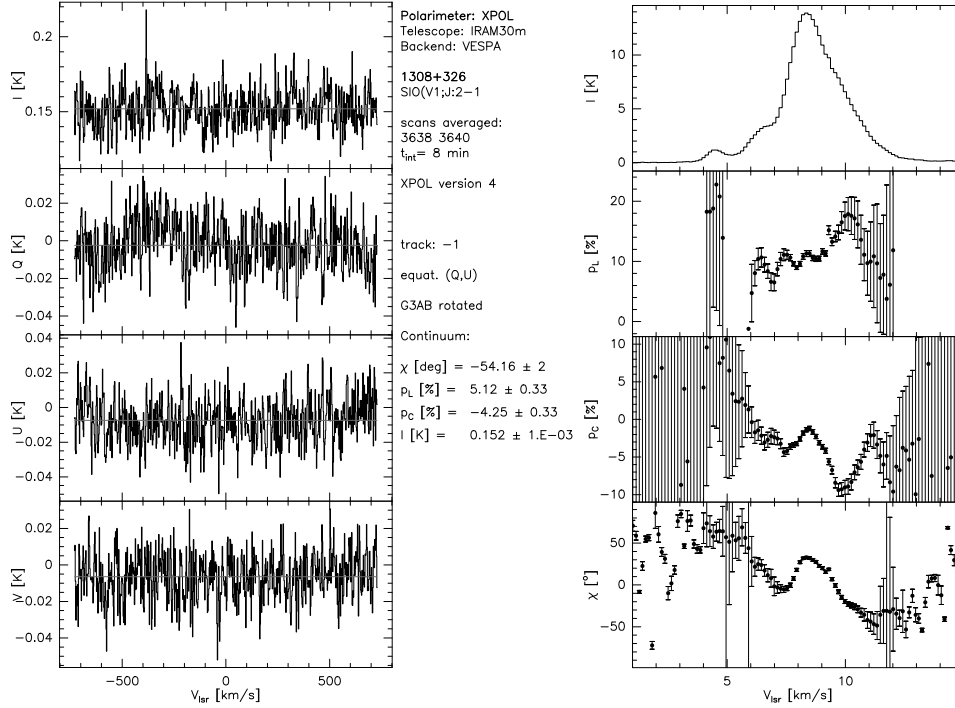


Fig. 4.— XPOL observations of a continuum (left) and spectral line source (right). The weakly polarized AGN 1308+326 was observed for 8 min. Its polarization parameters derived from averaging the spectral channels are listed on the right of the figure. The SiO star V Cam was observed with a spectral resolution of 80 kHz in the  $v = 2$ ,  $J = 2 \rightarrow 1$  maser transition at 86.243 GHz. The linear and circular polarization degrees,  $p_L$  and  $p_C$ , and the polarization angle  $\chi$  are well defined only in the spectral channels where the source is bright. Error bars are large when the total power is weak. Integration time 4 min.

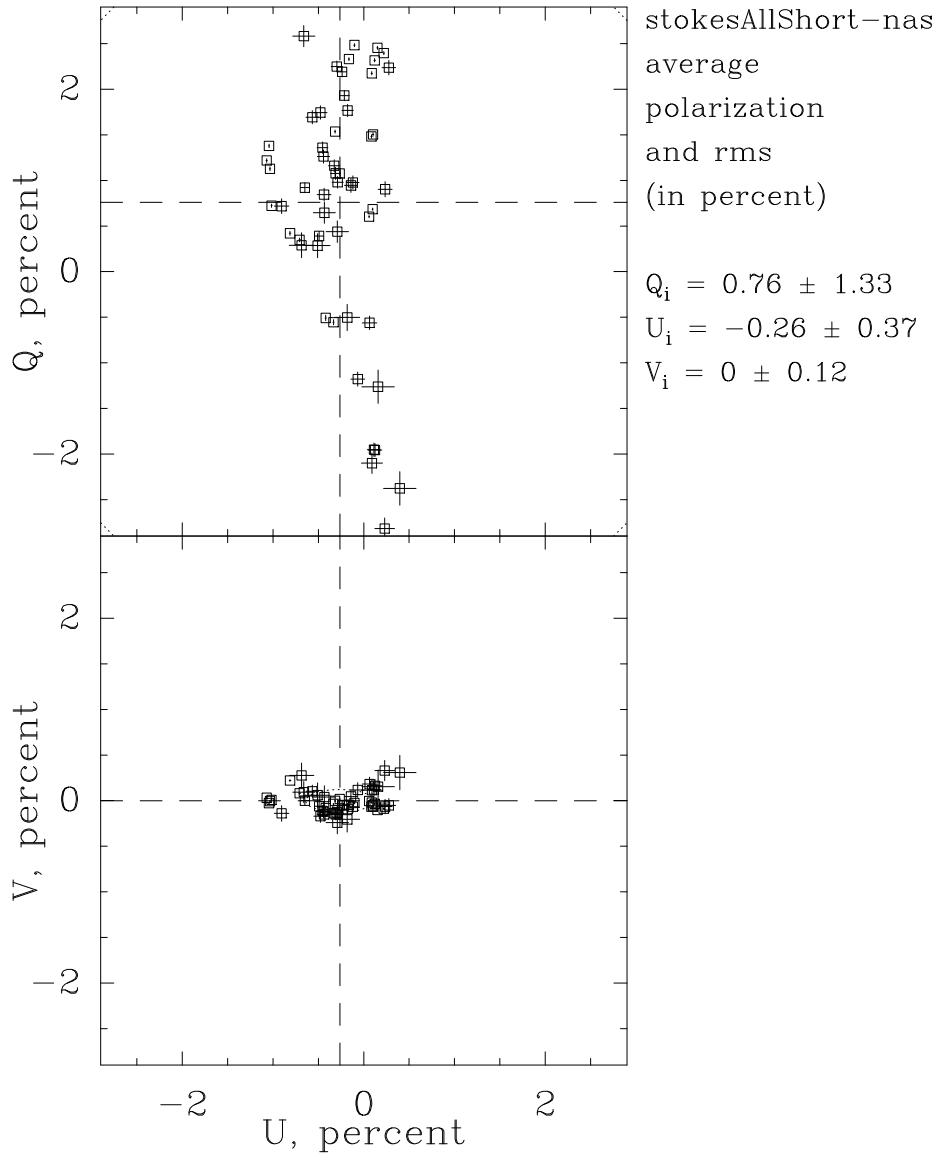


Fig. 5.— On-axis instrumental polarization as measured from Planets and HII regions. Observations were made during 2 weeks in July 2005 which included periods of very unstable and cloudy weather. All data are shown. The dashed lines indicate the mean values for the Stokes parameters  $Q$ ,  $U$ , and  $V$ .

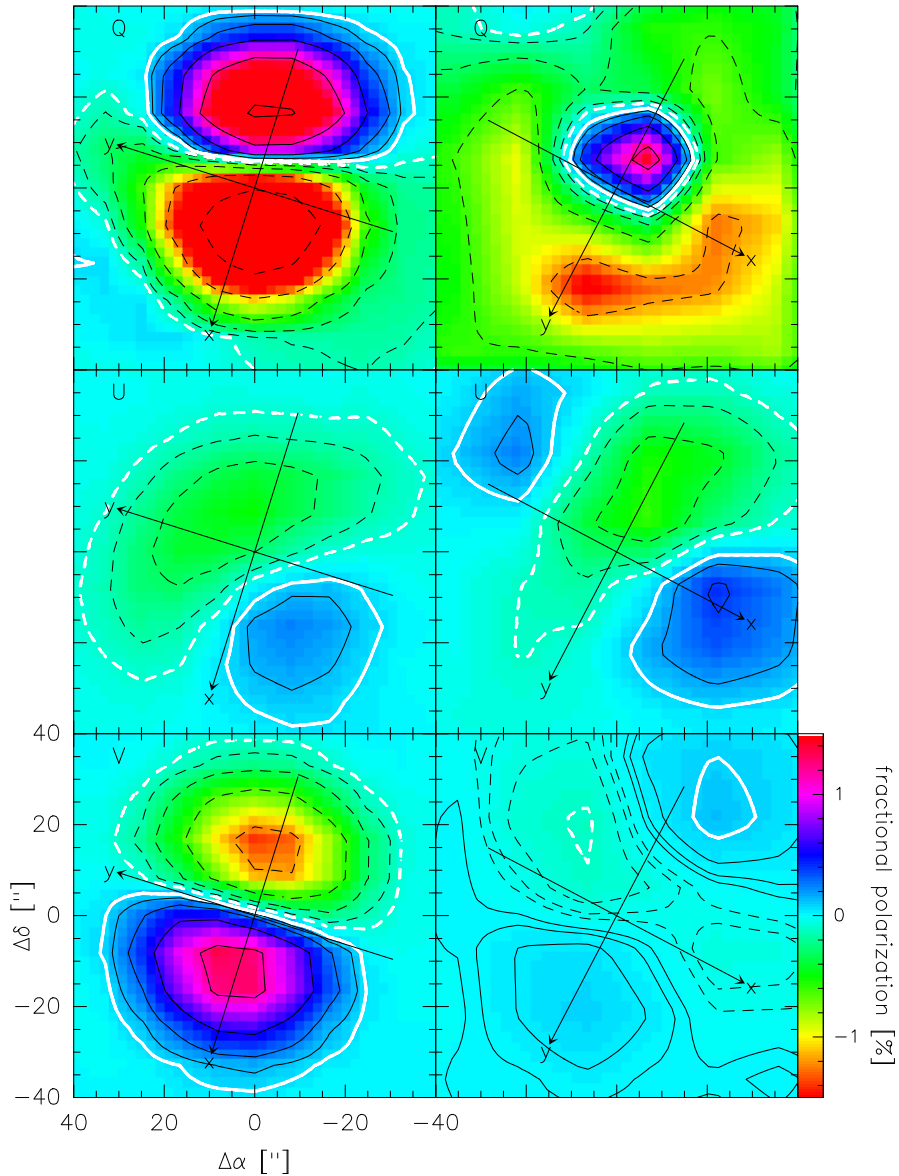


Fig. 6.— Beam maps of the Stokes parameters  $Q$ ,  $U$ , and  $V$  (from top to bottom) obtained at 86 GHz in 1999 (left) and 2005 (right). All maps have the same flux scale indicated on the lower right. Contours are drawn at 0.2, 0.4, 0.8, 1.6, and 3.2%, negative contours are dashed. The thick white contours are at  $\pm 0.1\%$ . The orientation of the  $x$  and  $y$  axes of the Nasmyth coordinate system  $\mathcal{K}_N$  is shown. Causes of the better results obtained in 2005 are described in the text (sect. 5.4).

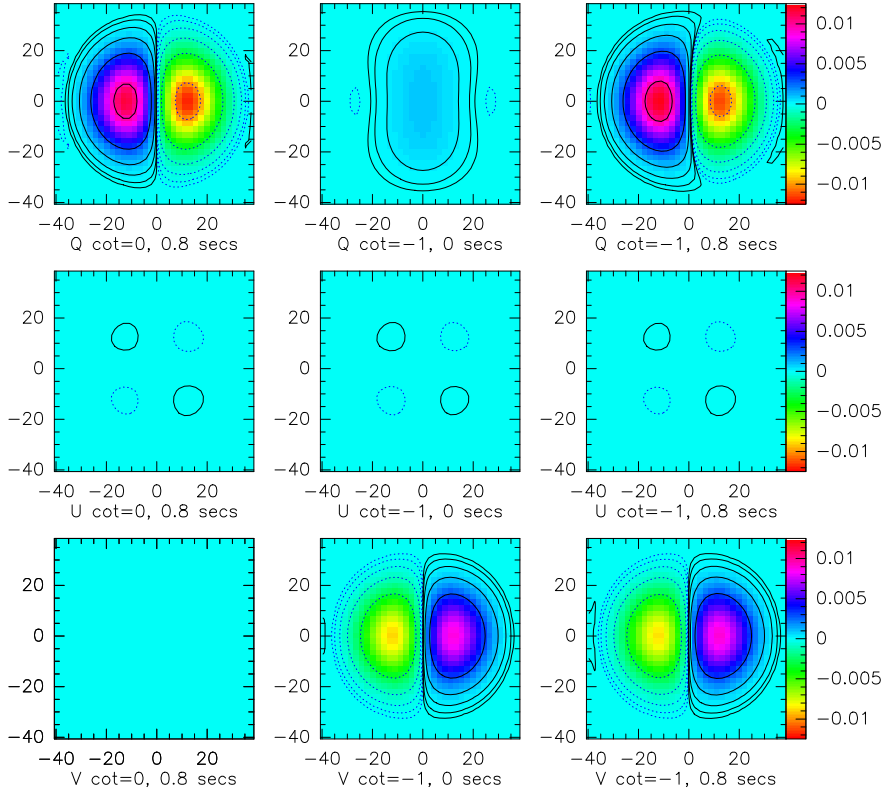


Fig. 7.— Simulation results for the far field cross-polarized sidelobes. The effects of changing the orientation of the polarization grid ( $cot$ ) and the pointing offsets (arc seconds) between the 2 receivers are shown in the 3 columns. Left column - offset 0.8 arc seconds, optimum orientation, middle column, - no offset, non-optimum orientation, right column - offset 0.8 arc seconds, non-optimum orientation. From top row to bottom row are displayed the Muller matrix elements  $M_{IQ}$ ,  $M_{IU}$ ,  $M_{IV}$ . The contours are at power levels relative to  $I$  of  $\pm 0.01, \pm 0.0036, \pm 0.001, \pm 0.00036, \pm 0.0001, \pm 0.000036$ .